High-Speed Tomographic PIV Measurements of Strain Rate Intermittency and Clustering in Turbulent Partially-Premixed Jet Flames

*Bruno Coriton and Jonathan H. Frank**

Combustion Research Facility, Sandia National Laboratories
Livermore, California 94551, USA

Colloquium on Turbulence

* *Corresponding Author: Jonathan H. Frank*
P.O. Box 969, MS. 9053
Livermore, CA 94551, USA
Fax: (925) 294-2595
jhfrank@sandia.gov

Color reproduction charges will be paid for those figures that in the revision stage cannot be reproduced in black and white without loss of clarity.

main text					**3923**
references	**17**			equiv. words	**332**
	Figure			**Caption**	**Figure total**
	height [mm]	# columns	equiv. words		
Fig. 1	46	1	124	7	131
Fig. 2	63	1	160	20	180
Fig. 3	52	1	137	14	151
Fig. 4	52	1	137	13	150
Fig. 5	65	1	166	29	195
Fig. 6	68	1	171	33	204
Fig. 7	78	1	193	23	216
Fig. 8	78	1	193	33	226
All figures					**1453**
	#text lines	#columns			
Table 1	5	1			**53**
Table 2	3	1			**38**
Total					**5799**

High-Speed Tomographic PIV Measurements of Strain Rate Intermittency and Clustering in Turbulent Partially-Premixed Jet Flames

Bruno Coriton and Jonathan H. Frank[*]

Combustion Research Facility, Sandia National Laboratories

Livermore, California 94551, USA

The effects of combustion on the strain rate field in turbulent jets was studied using 10 kHz tomographic particle image velocimetry (TPIV). We compared strain rate measurements in a well-studied, turbulent partially-premixed methane/air jet flame (*Sandia Flame C*) to measurements in a turbulent non-reacting air jet and a jet flame with significantly greater probability of localized extinction and intermittent blowoff. Since the jet exit Reynolds number of approximately 13,000 was nearly identical in the three jets, differences in the strain rate fields could be attributed to the presence (or absence) of a flame and its burning stability. Spatiotemporal characteristics of the strain rate field were analyzed. Overall, the strain rate norm was larger in the flames than in the non-reacting jet with the most stable flame having the largest values. In all three jets, the compressive strain rate was on average the largest of the three principal strain rates. At

high strain rates, the ratios of the compressive and extensive strain rate to the intermediate strain rate were similar to those found in isotropic incompressible turbulent flows. The three-dimensional velocity measurements were used to analyze the spatial distribution of strain rate clusters, defined as singly-connected groups of voxels where the strain rate magnitude exceeded a threshold value. The presence of a stable flame significantly attenuated the number of clusters of intermediate strain rate. Strain rate bursts, corresponding to sudden increases in the number of clusters, were identified in the three jets. The largest bursts in the non-reacting jet and the unstable flame contained twice as many clusters as in the stable flame. The temporal intermittency of the most intense strain rate clusters was analyzed using the time-series measurements. Clusters with strain rates greater than five times the standard deviation of the strain rate norm were highly intermittent.

Keywords: tomographic PIV, turbulent flames, strain rate, intermittency

1. Introduction

In turbulent flows, the occurrence and dynamics of fine-scale, intermittent, intense dissipative structures and their interplay with flames are not well understood [1-2]. Experimental studies of turbulent flames have greatly contributed to our understanding of turbulent combustion, but they are frequently limited to single-shot line or planar measurements and therefore unable to assess the three-dimensional transient nature of turbulent flows. Ultimately, the development of high-speed, 3-D imaging capabilities is required to fully capture the dynamics of turbulent combustion. The ability to perform high-speed

volumetric velocity field measurements is particularly valuable for studying the fluid dynamic strain field, which plays a central role in turbulent transport and turbulence-flame interactions.

On-going development of high-speed lasers and cameras opens new possibilities for experimental investigation of turbulent reacting flows. Tomographic particle image velocimetry (TPIV), introduced by Elsinga *et al.* [3], is an advanced PIV technique that provides instantaneous measurements of all three velocity components within a three-dimensional probe volume. TPIV has gained popularity within the fluid dynamics community where it has been applied to a broad range of studies from fundamental turbulence to applied-engineering problems [4]. Recently, single-shot [5] and high-speed [6] TPIV measurements in flames were demonstrated with potential to unveil new insights into turbulent combustion.

In the present study, we used high-speed TPIV measurements to investigate the effects of combustion on three-dimensional structures of elevated strain rate in turbulent jet flames. TPIV provides measurements of all nine components of the velocity gradient tensor, from which the deviatoric strain rate tensor can be determined [6]. We analyzed the strain rate tensor statistics in terms of its Euclidean norm and eigenvalues, also known as the principal strain rates, denoted s_1, s_2 and s_3, which are defined such that $s_1 \geq s_2 \geq s_3$ and $s_1 + s_2 + s_3 = 0$. The maximum and minimum principal strain rates, s_1 and s_3, correspond to the most extensive and compressive strain rate components, respectively. The ratio of the three principal strain rates along with the sign of s_2 provides insight into the structure of the strain field. High-speed TPIV measurements were used to study the temporal evolution of the strain rate field structure.

High-speed TPIV measurements were performed on the *Sandia flame C* [7], a well-studied, piloted partially-premixed CH_4/air jet flame with insignificant amount of localized extinctions. To investigate the effects of combustion on turbulent strain, we compare results in flame *C* to measurements in a turbulent non-reacting air jet and a second jet flame with significantly greater probability of localized

extinction and intermittent blowoff. The results are presented in the following three parts: *1)* characteristics of the principal strain rates, *2)* strain rate spatial clustering and *3)* the temporal intermittency of elevated strain rate structures.

2. Experimental Methods

2.1. Flow Conditions

High-repetition rate tomographic PIV was used to study the three jet flow conditions that are summarized in Table 1. Measurements in *Sandia flame C,* a piloted partially-premixed CH_4/air jet flame with a jet exit Reynolds number Re_{jet} of 13,000 [7], were performed at a distance of $y/D = 15$ (*viz.* $y = 112$ mm) above the nozzle exit. The measurements in flame *C* were compared to two additional cases: *1)* a turbulent jet of air (case *Air* in Table 1) with identical bulk jet exit velocity as in flame *C* and *2)* a second turbulent flame (labelled flame C_{LP}) with identical jet composition and Reynolds number as in flame *C* but with the pilot reduced to 26% of the original flow rate in flame *C*. Whereas flame *C* is moderately turbulent with rare localized extinctions, flame C_{LP} exhibits frequent localized extinction and intermittent blowoff that is rapidly followed by flame re-ignition. For all these cases, the coflow of air was set with an exit velocity of 0.9 m/s.

2.2. Experimental Apparatus

The layout of the experimental setup is depicted in Fig. 1. The TPIV system is identical to that used in Ref. [6] and consisted of a high speed diode-pumped dual-head Nd:YAG laser and a set of four high speed CMOS cameras. Measurements were performed at a repetition rate of 10 kHz using a laser energy of 5 mJ/pulse across the probe volume. The pulse delay between laser heads was set to 10 μs in the *Air* jet and 8 μs in the flames. A pair of cameras was positioned on each side of the laser beam with

two cameras positioned at 20 degrees with respect to the *z-axis* and the other two cameras at 45 degrees. The cameras were operated at 20 kHz in a frame straddling mode using a 896x800 px^2 region of the detector with a projected pixel size of approximately 15 μm/px. Jet and coflow were both seeded with 0.3 μm aluminum oxide particles. Light scattering from the alumina particles was imaged onto each camera using identical camera lenses and Scheimpflug mounts to compensate for the displacement of the imaging plane. The camera lenses were stopped down to f/16 and f/24 to obtain the necessary depth of field across the probe volume. Computation of the velocity vectors consisted of: *1)* smoothing (3x3 px^2 Gaussian filter) and correcting the raw particle images for non-uniformity of particle scattering signals, *2)* reconstructing the particle volume distribution using a Multiplicative Algebraic Reconstruction Tomography (MART) algorithm [3], *3)* calculating the velocity vectors by iterative volume cross-correlation for a final volume interrogation size of 24x24x24 vx^3 with 75% overlap and *4)* removing/replacing spurious vectors identified via an outlier detection method and reducing the measurement noise with a spatial filter based on a penalized least-square method [8] with a parametric smoothing strength of 2.0. The probe volume size was 16.5x12.3x2.5 mm^3 and contained 169x 126x26 vectors with 98.4 μm spacing.

2.3. Velocity Measurement Uncertainty

Uncertainty in the 10 kHz TPIV measurements was first evaluated using a steady laminar partially-premixed counterflow flame. A premixed stream of dimethyl-ether (DME) and air of equivalence ratio 3.6 was counterflowing against a stream of air with a 16 mm nozzle separation. Bulk velocities at the nozzle exits were 3.9 m/s. The 12.3 mm-high probe volume was centered between the nozzles. Laminar counterflows provide a well-characterized velocity field with a velocity gradient along the burner axis. The TPIV uncertainty is readily determined in a steady flow field since any variations in the measured velocities or velocity gradients are attributed to measurement error. The TPIV

configuration was identical to that of the measurements in the turbulent jets except that the laser head pulse delay was increased to 50 μs to account for the lower velocities. Figure 2a shows mean centerline profiles of all three velocity components from 500 single-shot velocity measurements. The length of the error bars displayed every 12 data points along the curves in Fig. 2 corresponds to twice the standard deviation at these points. Because of heat release in the flame, the axial velocity has an inflection point near the stagnation plane at $Y \sim 0$ mm. The velocity standard deviations were 3-to-8 cm/s in the reactants and increased to 12 cm/s in the flame. The velocity derivatives are more sensitive to noise degradation. In Fig. 2b, the mean divergence is nearly zero in the reactants and displays two peaks in the flame because of dilatation. The uncertainty of the divergence measurements was ±150/s in the reactants and ±230/s in the flame. The standard deviations of the principal strain rates in the reactants and flame were respectively 110/s and 150/s for s_1 and 160/s and 240/s for s_3. The profiles in Fig. 2 are consistent with velocities in reactive counterflow jets and demonstrate the ability of TPIV to measure a 3-D velocity field in a flame. The slightly larger errors in the flame zone may be attributed to thermophoretic diffusion and beam steering.

In turbulent flows, additional sources of errors are expected because of flow acceleration and under-resolved turbulence lengthscales [6]. Distributions of divergence in incompressible flows are often used to evaluate the extent of measurements errors. In the incompressible *Air* jet of Table 1, measurement errors caused the local divergence to deviate from zero with an uncertainty of ±900/s. Principal strain rates in the presumably irrotational air coflow were as large as 1,000/s. These errors are however relatively small in comparison to the strain rates that are of greatest interest in this study.

3. Results and Discussion

The effect of combustion on the turbulent strain rate field was investigated by comparing TPIV measurements in the three flow conditions in Table 1. The fluid dynamics properties of the three jets were nearly identical and, therefore, differences in the strain rate fields could be attributed to the presence (or absence) of a flame and its burning stability. The statistical analysis of each flow condition was performed using a 200 ms time sequence of TPIV measurements acquired at 10 kHz.

3.1. Strain Rate Magnitude and Principal Strain Rates

To investigate the effects of combustion on the strain rate field, we first consider the distributions of the norm of the strain rate tensor: $|s| = |s_1^2 + s_2^2 + s_3^2|^{0.5}$, which provides a measure of the total strain rate and is related to the kinetic energy dissipation as $\varepsilon = 2\nu|s|^2$. Probability density functions (PDFs) of $|s|$ are plotted in Fig. 3 for the three flow conditions of Table 1. All of the PDFs of $|s|$ are skewed with long tails that extend toward large strain rate values, indicative of the intermittency of the most intense strain rates. The strain rate magnitude is enhanced by combustion with the tail of the PDF of $|s|$ extending to the largest values in flame *C* and intermediate values in flame C_{LP}. For all three cases, values of the strain rate standard deviation, $|s|' = \langle|s|^2\rangle^{0.5}$, are given in Fig. 3 and Table 2. Extreme values of $|s|$ that exceed five times their respective standard deviations (Table 2) only occur in approximately 1% of the measurements. However, these rare events may have a disproportionate impact on the reaction zones of the flames.

The effects of combustion on the structure of the strain rate tensor are investigated using an analysis of the principal strain rates in the three jet flows. Figure 4 shows PDFs of the normalized intermediate principal strain rate: $s_2^n = s_2/(|s|^2/6)^{0.5}$, where the factor $\sqrt{6}$ is introduced to bound the normalization within [-1;1]. The sign of s_2^n indicates whether the local strain rate has one compressive axis, $s_2^n > 0$, or two compressive axes, $s_2^n < 0$. To elucidate the structural differences in high strain rate regions, we

compare PDFs of s_2^n conditioned on large strain rates, $|s| > 5|s|'$, with those that include all regions of non-zero strain rate, $|s| > 0$. The PDFs for $|s| > 5|s|'$ are significantly more skewed than for $s_2^n > 0$ such that s_2 is predominantly positive in regions of high strain rate for all of the flows. Therefore, the intense strain rates in the reacting and non-reacting jet flows are preferentially sheet-forming with a single axis of compressive strain.

Further insight on the state of the strain rate field can be gained from the relative ratios between the three principal strain rates, s_1:s_2:s_3, which can be determined from the values of s_2^n. Previous studies based on simulations of incompressible turbulent flows predict that PDFs of s_2^n are skewed towards positive values at high strain rates, with the most probable value of $s_2^n = 0.6$, corresponding to strain rate ratios of 2.25:1:-3.25 [9]. Ashurst *et al.* [9] indicate that this dependence of the conditional PDF shape on strain rate is a generic structure of intense turbulence that appears in isotropic turbulence and turbulent flows with shear. Other numerical studies [10-11] and recent pseudo-3D velocity measurements in the far-field of a low Reynolds number jet flame [12] indicate that the presence of shear tends to decrease the most probable value of s_2^n to less than 0.6. For all three flow conditions, the PDFs of s_2^n conditioned on $|s| > 0$ in Fig. 4 show that the most probable value of s_2^n is approximately 0.2, corresponding to strain rate ratios of approximately 8:1:-9. These ratios indicate that the extensive and compressive strain rates dominate over the intermediate strain rate and, overall, the strain rate field tends to be planar in these turbulent non-reacting and reacting jets. However, regions of high strain rate exhibit different properties. In Fig. 4, the PDFs of s_2^n conditioned on large values of strain rate, $|s| > 5|s|'$, show a shift in the most probable value of s_2^n toward 0.6, as found in isotropic turbulence. This shift is slightly greater for the non-reactive case than for the flames.

3.2. Strain Rate Clustering

To understand the structure of the strain rate field, we compare the topology of strain rate in the *Air* jet with that of flames C_{LP} and *C*. Three-dimensional rendering of strain rate isosurfaces in the turbulent *Air* jet and the turbulent flame *C* are presented in Figs. 5a and 5b, respectively. The examples in Fig. 5 are illustrative of the strain rate topology in the *Air* jet and flame *C*. For each case, the same single-shot measurement is displayed using three increasing levels of strain rate isosurfaces, namely $|s|$=6,000/s (left images), $|s|$=9,000/s (middle images) and $|s|$=12,000/s (right images). Figure 5 shows the qualitative differences between the *Air* jet and flame *C* as well as the effect of varying the isosurface threshold that is used to represent three-dimensional flow structures.

Strain rate structures exhibit a large variety of sizes and shapes in both the non-reacting and reacting flows. The shapes of the structures are more complex than the lamella-like structures of scalar dissipation layers in turbulent jet flames [13]. In the *Air* jet in particular, bursts of strain rate structures are observed (Fig.5a). Such events are also observed in flame *C* but include fewer structures. In flame *C*, however, an elongated sheet-like structure spans the height of the probe volume (Fig.5b) and is aligned along the shear layer. Structures of high strain rate and vorticity are known to align along the reaction zone in turbulent jet flames [14].

As the strain rate isosurface level increases, the number of structures and their size decrease. In flame *C*, the large sheet-like structure remains identifiable across the 6,000/s-12,000/s range of strain rate isosurfaces. However, as the strain rate threshold increases, many of the small structures disappear. This dependence of the topology on the strain rate threshold indicates that using a single threshold value provides an incomplete representation of the strain rate field. As a result, the strain rate field topology must be analyzed as a function of the strain rate threshold, denoted $|s_{thrs}|$.

The number and volume of structures in the strain rate field are quantified as a function of $|s_{thrs}|$ using a clustering analysis. For a given value of $|s_{thrs}|$, a *cluster* is defined as a singly-connected group

of voxels where $|s| > |s_{thrs}|$ [15]. The size and shape of the clusters vary greatly with $|s_{thrs}|$, as can be inferred from the isosurfaces in Fig. 5. For a given snapshot, clustering is quantified in terms of the number of clusters, N_c, appearing in the probe volume and the fraction of the probe volume occupied by clusters, V_c. The ensemble-averages of N_c and V_c are plotted as function of $|s_{thrs}|$ in Fig. 6 for all three turbulent jet cases.

Figure 6a provides insight into the structure of the strain rate field, which consists of many local maxima and minima. For a very low value of $|s_{thrs}|$ such that it is below most of the minima, there is very little segmentation of the field, and the number of clusters is small. As $|s_{thrs}|$ increases and exceeds the local minima, the field becomes segmented and $<N_c>$ systematically increases. Once $|s_{thrs}|$ is sufficiently large to identify the majority of local strain rate peaks, $<N_c>$ reaches a maximum (e.g. $\langle N_{C,Air} | |s_{thrs}| = 5{,}000/s \rangle$ in Fig. 6a). Further increases in $|s_{thrs}|$ eliminate much of the strain rate field, and the only remaining structures are the extreme maxima, as seen in Fig. 5. As a result, $<N_c>$ decreases. A low profile of $<N_c>$ in Fig. 6a is indicative of a well-connected strain rate field with few local maxima and minima, whereas a high profile of N_c corresponds to a scattered spatial distribution of intermediate-to-high strain rate clusters. Accordingly, Fig. 6a indicates that the strain rate field is better connected in the stable flame *C* than in the two other cases. In the *Air* jet and flame C_{LP}, $<N_c>$ exceeds 100 for $|s_{thrs}| > 4{,}000/s - 5{,}500/s$. For $|s_{thrs}| > 6{,}000/s$, $<N_c>$ decreases faster in the *Air* jet than in flame C_{LP} indicating that local strain rate maxima are typically of higher magnitude in flame C_{LP} than in the *Air* jet. For elevated strain rate ($|s_{thrs}| > 8{,}000/s$), $<N_c>$ becomes comparable in flames C_{LP} and *C*.

A more complete picture of the cluster characteristics emerges when the results of Fig. 6a are combined with the profiles of $<V_c>$ in Fig. 6b. Figure 6b shows that clusters occupy a decreasing fraction of the probe volume as $|s_{thrs}|$ increases. On average, strain rate clusters occupy a larger volume in the two flames than in the *Air* jet. For intermediate strain rates (3,000/s-6,000/s), flame *C* has the

largest volume occupied by clusters and the fewest number of clusters (Fig. 6a). Therefore, individual clusters of intermediate strain rate are on average larger in flame *C* than in flame C_{LP} or the *Air* jet.

3.3. Strain Rate Bursts and Temporal Intermittency

The spatial intermittency of small-scale turbulence has been studied more extensively than its temporal intermittency [2]. Previous experimental studies of turbulent intermittency have focused on the spatial intermittency of the velocity components and their derivatives [16]. However, the temporal intermittency of the strain rate field may have significant implications in turbulent combustion. For example, turbulent flames can withstand transient strain rates that are an order of magnitude larger than the extinction strain rate of the corresponding steady laminar flame [6]. The level of localized extinction in turbulent flames may well depend on the intermittency and lifetime of these very high strain rates. High-speed three-dimensional measurements of the velocity field are required to fully capture the intermittency of the strain rate field. The temporal intermittency of the intense strain rate clusters was investigated using 200 ms-long time-series of TPIV measurements at 10 kHz.

Images displayed in Fig. 7 show 100 ms-long time-series of the number of clusters, N_c. Each column in the images corresponds to a profile of N_c as a function of the strain rate threshold, $|s_{thrs}|$, at a single instant in time. Each image row is a time series of N_c for a single value of $|s_{thrs}|$. The rapid modulation of the time traces in Fig. 7 is indicative of intermittent bursts of large numbers of strain rate clusters appearing simultaneously in the probe volume. In the *Air* jet and flame C_{LP}, for intermediate strain rates (3,000/s-6,000/s), bursts of over 200 clusters can rapidly appear in the probe volume, whereas, in flame *C*, the bursts rarely exceed 100 clusters. Burst dynamics may be related to the growth of the shear layer hydrodynamic instability, which is attenuated in turbulent jet flames [17].

An example of a burst of high strain rate clusters is shown for the *Air* jet in Fig. 5a, where structures of high strain rate (12,000/s) are embedded within clusters of intermediate strain rate (6,000/s). The

vertical profiles of the tallest peaks in Fig. 7 indicate that large bursts of high strain rate are frequently coincident with bursts of intermediate strain rate.

To characterize the intermittency of strain rate clusters, we evaluated the probability of the probe volume containing at least one cluster with strain rate exceeding $|s_{thrs}|$, $P(N_c \geq 1, |s_{thrs}|)$. Figure 8a shows $P(N_c \geq 1, |s_{thrs}|)$ plotted as a function of $|s_{thrs}|$ in the range 6,000/s-20,000/s for the non-reacting flow and flames. For all three flow conditions, clusters for $|s_{thrs}| \leq 5|s|'$ (Table 2) are almost continuously present in the probe volume. The probability that structures of higher strain rate appear in the probe volume decreases rapidly with increasing $|s_{thrs}|$. Recall that, in Fig. 3, values of $|s|$ greater than $5|s|'$ represent only 1% of the spatiotemporal velocity measurements. These clusters of extremely large strain rate are statistically insignificant but there effects on flames may not be negligible.

The time-series measurements enable determination of the time intervals between appearances of clusters above $|s_{thrs}|$ and the duration of these occurrences. The mean values of these quantities for the three turbulent jets are plotted in Fig. 8b. To distinguish real flow structures from apparent structures that resulted from noise, we only considered structures that persisted for a minimum of two frames. Therefore, any structure that didn't persist for at least 0.2 ms was considered noise and discarded. Clusters are convected in and out of the probe volume and can be produced or dissipated inside the probe volume. Clusters of intermediate strain rate, $|s_{thrs}| \leq 5|s|'$, are nearly always present in the probe volume and thus their mean time interval between appearances is approximately zero. However, high strain rate clusters are temporally intermittent. According to Fig.8b, as strain rate increases, the time interval between appearances increases and the duration of the clusters decreases. The mean flow residence time across the probe volume is approximately 1.3 ms in the *Air* jet, 0.8 ms in flame C_{LP} and 0.6 ms in flame *C*. The residence time of very high strain rate clusters falls below the mean flow residence time. These structures were observed to form or dissipate within the probe volume. The

interaction time between these structures of extreme strain rates and the flame reaction zone is critical for understanding localized extinction in turbulent flames.

4. Conclusions

The effects of combustion on strain rate properties, intermittency and clustering were investigated using 10 kHz tomographic PIV to measure the temporal evolution of the strain rate field in three dimensions. Measurements in stable and unstable partially premixed jet flames of jet Reynolds number ~13,000 were compared to a turbulent non-reactive jet.

The findings are summarized as follows:

- The magnitude of the strain rate increases in turbulent reactive jets. In the non-reacting and reacting jets, the compressive strain rate is on average the largest principal strain rate, especially in regions of elevated strain rate. On average, the compressive and extensive strain rates are significantly larger than the intermediate principal strain rate, indicating a locally planar strain. At elevated strain rates, the principal strain rate ratios in the flames approach those found in isotropic incompressible turbulence.

- Clusters of intermediate strain rate tend to occupy a larger volume in the stable flame than in the other two cases. The number of clusters in the stable flame is also typically lower than in the other cases.

- Strain rate bursts, corresponding to sudden increases in the number of clusters, were identified in the three jets. However, bursts in the non-reacting jet and the unstable flame could contain twice as many clusters as in the stable flame.

- Clusters of strain rate magnitude less than $5|s|'$ are continuously present in the probe volume. Structures of higher strain rates become highly temporally intermittent.

These results show the multi-faceted effects of combustion on the magnitude, structure, and intermittency of the strain rate field. The flame with localized extinctions and blowoff has strain rate characteristics that are a mixture between those of the fully reacting flame and the air jet. These insights into the strain rate field are highly relevant to the development and validation of turbulent combustion models and LES sub-models.

Acknowledgments

The authors thank Mr. Erxiong Haung for technical assistance in the laboratory. This research was supported by the U.S. Department of Energy, Office of Basic Energy Sciences, Division of Chemical Sciences, Geosciences, and Biosciences. Sandia National Laboratories is a multiprogram laboratory operated by Sandia Corporation, a Lockheed Martin Company, for the U.S. Department of Energy under contract DE-AC04-94-AL85000.

References

[1] A., Kerstein, Proc. Combust. Inst. 29 (2002) 1763-1773.

[2] K.R., Sreenivasan, Flow Turbul. Combust. 72 (2004) 115-131.

[3] G.E., Elsinga. B., Wieneke, F., Scarano, B.W., van Oudheusden, Exp. Fluids 41 (2006) 933-947.

[4] F., Scarano, Meas. Sci. Technol. 24 (2013) 012001.

[5] J., Weinkauff, D., Michaelis, A., Dreizler, B., Bohm, Exp. Fluids 54 (2013) 1624-1629.

[6] B. Coriton, A.M., Steinberg, J.H., Frank, Submitted to Exp. Fluids (09/2013).

[7] R.S., Barlow, J.H., Frank, Proc. Combust. Inst. 27 (1998) 1087-1095.

[8] D., Garcia, Computational Statistics and Data Analysis 54 (2010) 1167-1178.

[9] W.T., Ashurst, A.R., Kerstein, R.M., Kerr, C.H., Gibson, Phys. Fluids 30 (1987) 2343-2353.

[10] J.G., Brasseur, W., Lin, Fluid Dynamic Research 36 (2005) 357-384.

[11] J.C., Isaza, L.R., Collins, J. Fluid Mech. 678 (2011) 14-40.

[12] M. Gamba, N.T., Clemens, O.A., Ezekoye, Meas. Sci. Technol. 24 (2013) 024003.

[13] J.H., Frank, S.A., Kaiser, Exp. Fluids 49 (2010) 823-837.

[14] J.E., Rehm, N.T., Clemens, Proc. Combust. Inst. 22 (1998) 1113-1120.

[15] T., Sanada, Phys. Rev. A 44 (1991) 106480.

[16] K.R., Sreenivasan, R.A., Antonia, Annu. Rev. Fluid. Mech. 29 (1997) 435-472.

[17] J.E., Rehm, N.T. Clemens, Combust. Flame 116 (1999) 615-626.

Tables

Cases	φ_{jet}	Re_{jet}	V_{jet} *(m/s)*	V_{Pilot} *(m/s)*
Air	0.0	13,500	27.5	0.0
C_{LP}	6.0	13,000	27.5	1.8
C	6.0	13,000	27.5	6.8

Table 1 – Summary of flow conditions

Cases	*Air*	C_{LP}	*C*
$\|s\|'$	1,535/s	1,825/s	2,094/s
$5\|s\|'$	7,675/s	9,125/s	10,470/s

Table 2 – Standard deviations of the strain rate norm

Figures

Figure 1 – Experimental Setup for high-repetition rate tomographic PIV.

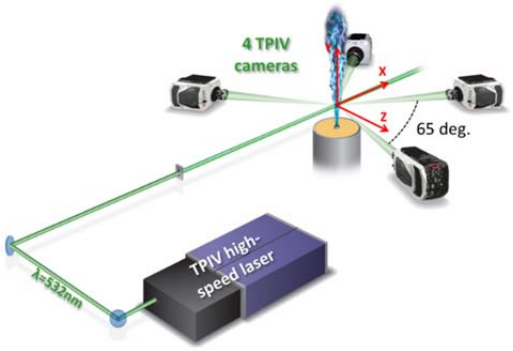

Figure 2 – Centerline profiles of a) velocity components and b) divergence and extensive and compressive strain rates in a laminar counterflow flame.

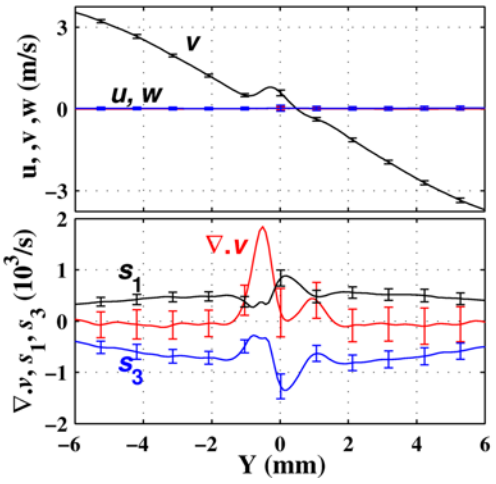

Figure 3 – PDFs of the norm of the strain rate in the three turbulent jet conditions.

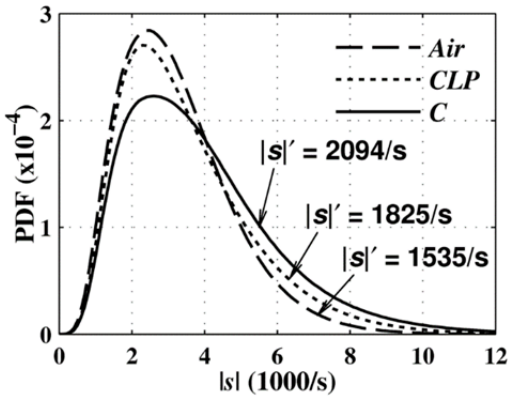

Figure 4 – PDFs of normalized intermediate principal strain rate, s_2^n, conditioned on $|s| > 0$ or $|s| > 5|s|'$.

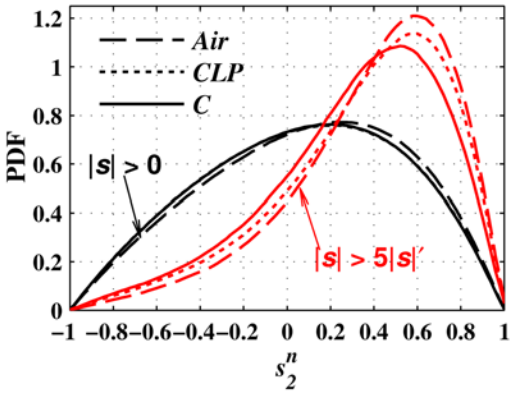

Figure 5 – Rendering of strain rate isosurfaces for $|s|$=6,000/s (left), $|s|$=9,000/s (middle) and $|s|$=12,000/s (right) in a) the turbulent *Air* jet and b) flame *C*. Box dimensions: LxHxW = 10.7x12.3x2.5 mm^3.

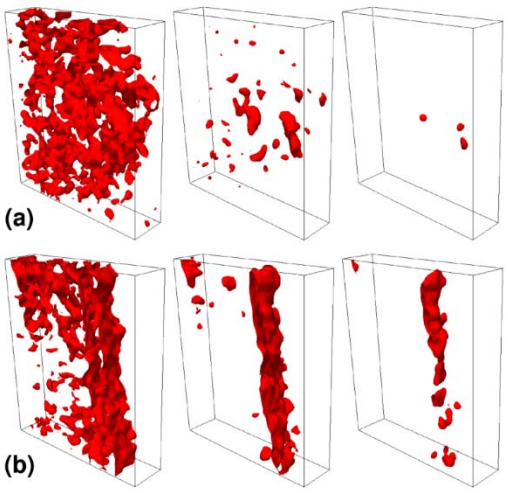

Figure 6 – Clustering statistics in the three turbulent jet conditions of Table 1. a) Average number of clusters in the probe volume per snapshot. b) Average fraction of probe volume occupied by clusters (logarithmic *y*-axis).

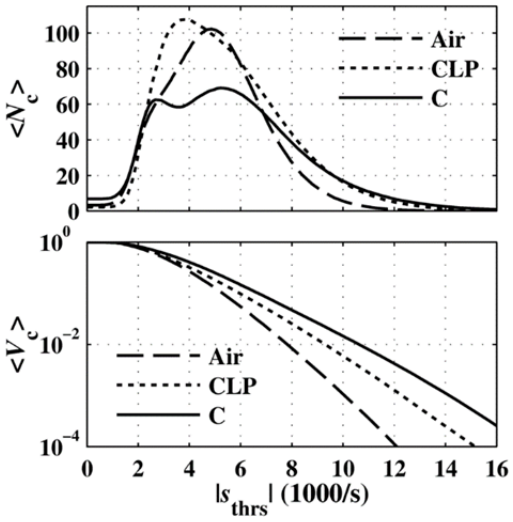

Figure 7 – Time series of the number of clusters, N_c, as a function of strain rate threshold in the three flow conditions of Table 1.

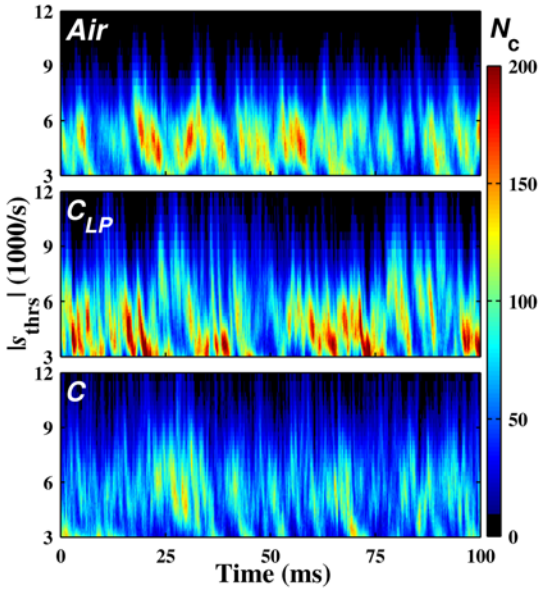

Figure 8 – a) Probability of $N_c \geq 1$ (logarithmic *y*-axis). b) Mean time interval (black) between appearances of strain-rate clusters having a magnitude greater than $|s_{thrs}|$ and mean duration (red) of these occurrences (logarithmic *y*-axis).

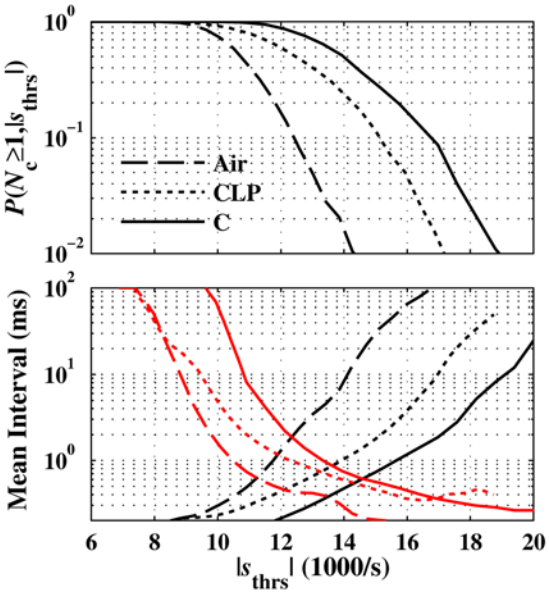

List of Figure Captions

Figure 1 – Experimental Setup for high-repetition rate tomographic PIV.

Figure 2 – Centerline profiles of a) velocity components and b) divergence and extensive and compressive strain rates in a laminar counterflow flame.

Figure 3 – PDFs of the norm of the strain rate in the three turbulent jet conditions.

Figure 4 – PDFs of normalized intermediate principal strain rate, s_2^n, conditioned on $|s| > 0$ or $|s| > 5|s|'$.

Figure 5 – Rendering of strain rate isosurfaces for $|s|$=6,000/s (left), $|s|$=9,000/s (middle) and $|s|$=12,000/s (right) in a) the turbulent *Air* jet and b) flame *C*. Box dimensions: LxHxW = 10.7x12.3x2.5 mm^3.

Figure 6 – Clustering statistics in the three turbulent jet conditions of Table 1. a) Average number of clusters in the probe volume per snapshot. b) Average fraction of probe volume occupied by clusters (logarithmic *y*-axis).

Figure 7 – Time series of the number of clusters, N_c, as a function of strain rate threshold in the three flow conditions of Table 1.

Figure 8 – a) Probability of $N_c \geq 1$ (logarithmic *y*-axis). b) Mean time interval (black) between appearances of strain-rate clusters having a magnitude greater than $|s_{thrs}|$ and mean duration (red) of these occurrences (logarithmic *y*-axis).